RSC Advances

PAPER

View Article Online
View Journal | View Issue

Cite this: *RSC Adv.*, 2025, **15**, 23910

Engineering gold nanoparticles-infused silica aerogel composite for trace mercury adsorption

Subhash Kumar Sharma, †[a] Eitan Yosef,†[b] Hadas Mamane[b] and Rajnish Kumar *[ac]

Mercury (Hg) contamination in water poses severe environmental and health risks, necessitating efficient and scalable remediation technologies. We report a novel gold nanoparticle-doped silica aerogel (Au-AG) composite synthesized *via* supercritical fluid impregnation, designed to harness the high surface area and porosity of silica aerogels alongside the strong Hg-binding affinity of gold nanoparticles (Au-NPs). The resulting composite exhibits robust structural integrity and a characteristic purple hue, indicating uniform dispersion of Au-NPs. Adsorption experiments at environmentally relevant Hg concentrations show that uptake follows Langmuir isotherm behavior and pseudo-second-order kinetics, indicative of monolayer chemisorption and rapid adsorption rates. The Au-AG composite achieves up to 85% Hg removal within 24 hours and a maximum adsorption capacity of 12.82 mg g^{-1} at ppb-level Hg concentrations, outperforming conventional materials such as activated carbon, thiol-functionalized resins, and undoped silica aerogels under similar conditions. The composite's structural integrity and chemical stability indicate potential for regeneration and reuse in cyclic adsorption processes, making it a promising candidate for sustainable water purification technologies. Moreover, the synthesis approach is compatible with scalable and sustainable production, reinforcing its applicability in real-world water purification systems. These findings position the Au-AG composite as a high-performance and scalable solution for trace-level mercury remediation in contaminated water, advancing sustainable environmental technologies.

Received 19th February 2025
Accepted 1st July 2025

DOI: 10.1039/d5ra01213a

rsc.li/rsc-advances

1. Introduction

Mercury (Hg) is a highly toxic, persistent contaminant with a strong tendency to bioaccumulate, posing global environmental and public health risks.[1] Geogenic sources like volcanic eruptions and oceanic degassing release 500–800 metric tons of mercury annually.[2] However, human activities, especially industrial processes,[3] have increased emissions significantly, with the UNEP estimating over 2000 metric tons released yearly, largely from coal combustion. Mercury exposure mainly occurs through methylmercury in contaminated fish, impacting human health with severe neurological, cardiovascular, and immune effects.[4] High-risk groups include fetal development and communities consuming fish high in mercury, like tuna. Mercury emissions travel globally, affecting remote regions like the Arctic, harming ecosystems and species such as bald eagles, polar bears, and panthers. In terrestrial environments, mercury also accumulates, impacting species like bats through contaminated prey. Economically, mercury exposure leads to costly cognitive impairments, and fishing communities face food insecurity and cultural loss due to dietary mercury restrictions.[5]

Mercury exists as elemental (Hg^0), inorganic (Hg^{2+}), and organic (methylmercury, MeHg) forms, each with distinct properties and removal challenges.[6,7] Elemental mercury disperses easily in the air, complicating containment; inorganic mercury dissolves in water, binding with other compounds; and methylmercury, the most toxic, biomagnifies in food chains, impacting wildlife and human health.[8] Removal techniques must be tailored to each form, with elemental mercury removal (*e.g.*, activated carbon adsorption) often ineffective for methylmercury, complicating removal efforts and driving up costs, especially in resource-limited areas. Traditional methods like chemical precipitation, membrane filtration, ion exchange, and adsorption offer varied benefits and drawbacks: chemical precipitation forms insoluble mercury compounds but produces challenging sludge, membrane filtration can remove mercury ions but is energy-intensive and prone to fouling, ion exchange captures ions effectively but requires costly regeneration, and adsorption, while affordable for elemental mercury, is less efficient for methylmercury and requires large adsorbent quantities, making comprehensive mercury removal both costly and complex.[9]

[a]*Department of Chemical Engineering, Indian Institute of Technology Madras, Chennai-600036, India. E-mail: rajnish@iitm.ac.in*

[b]*School of Environmental Engineering, Faculty of Mechanical Engineering, Tel Aviv University, Israel*

[c]*School of Sustainability, Indian Institute of Technology Madras, Chennai-600036, India*

† These authors contributed equally and are co-first authors.

Meeting strict mercury limits (*e.g.*, 2 ppb per EPA, 1 ppb per WHO) is difficult for traditional removal methods, which often struggle with trace levels and require costly multistage processes to meet compliance.[10] Effective systems demand continuous operation and maintenance, as they are sensitive to pH, temperature, and contaminant variability, particularly in complex industrial effluents. Worker safety in high-mercury environments is a concern, with OSHA (Occupational Safety and Health Administration) reporting mercury levels five times above safe limits, necessitating strict safety protocols. Advances in nanotechnology, like aerogels[11] and gold nanoparticles (Au-NPs), show promise for mercury removal due to high surface areas and strong mercury-binding efficiency.[12] Au-NPs impregnated silica aerogels, for instance, merge aerogel durability with the adsorption capacity of Au-NPs, achieving over 90% mercury removal and up to 200 mg g^{-1} adsorption capacity, though challenges in production costs, scalability, and nanoparticle agglomeration remain.[13] Other composites, like MoS_2/graphene oxide aerogels with Fe_3O_4 magnetic NPs, have achieved 1527 mg g^{-1} adsorption but still face scalability issues.[14] However, these results were obtained at significantly higher initial mercury concentrations (100–500 ppm), which are not typical of natural water systems. In contrast, this study focuses on adsorption performance at trace-level mercury concentrations (10–100 ppb), which are more relevant to real-world contamination scenarios. Au-NPs silica aerogels also have potential in catalysis,[15] sensing, and shielding applications, with supercritical CO_2 impregnation aiding in versatile metal incorporation.[16]

Silica aerogels impregnated with gold nanoparticles[17] (Au-NPs) using supercritical carbon dioxide ($scCO_2$) offer an effective solution for mercury (Hg) adsorption from water, addressing mercury's environmental risks due to toxicity and bioaccumulation. The high surface area and porosity of silica aerogels, combined with gold's affinity for mercury ions, enable efficient adsorption in industrial and natural water sources.[18] $scCO_2$ uniformly disperses Au-NPs within the aerogel matrix, preserving structure and maximizing mercury interaction.[19] Studies show that silica-based hybrids, like silica–carbon nanotube composites,[20–22] offer high Hg^{2+} adsorption capacity, surpassing traditional methods. Gold-enhanced aerogels exhibit robust adsorption kinetics and monolayer adsorption, following pseudo-second-order models, indicating chemisorption. Additional innovations, such as sulfur-functionalized silica for vapor-phase remediation and mercaptoamine-functionalized[23] silica for wastewater, highlight the adaptability of these materials.[24] Hydrophobic silica aerogels[25] also adsorb organic compounds, while modified silicas can capture CO_2, suggesting broad applications beyond metal remediation, including in environmental and analytical applications.

This research aims to develop a highly efficient mercury adsorbent by synthesizing a silica aerogel impregnated with gold nanoparticles (Au-NPs) using supercritical CO_2 ($scCO_2$). It focuses on characterizing the composite's properties, analyzing adsorption kinetics, and evaluating mercury-binding mechanisms to deliver a scalable solution for industrial mercury removal and environmental remediation. By offering a sustainable alternative to traditional methods, the study advances heavy metal adsorption and supports next-generation adsorbent development for diverse applications.

2. Materials and methods

2.1. Chemicals

Cabot P400 silica aerogel was provided as a gift by Cabot. Gold chloride ($AuCl_2$) was obtained from SRL Chemicals, India. Carbon dioxide (CO_2) gas, with a purity of 99.995%, was sourced from Indogas, India, for the supercritical impregnation. The ethanol (EtOH), hydrochloric acid (HCl), and nitric acid (HNO_3) reagents were obtained from SRL Chemicals, India. Merck, India supplied mercury chloride ($HgCl_2$).

2.2. Procedure for Au-AG aerogel synthesis

The synthesis protocol was designed with scalability in mind, using industrial-grade silica aerogel and supercritical CO_2 a process already used at commercial scale in other sectors. The Cabot P400 silica aerogel (4 g) was impregnated by spraying it with $AuCl_2$ (160 mg) dissolved in EtOH (3.2 mL) on a metal sieve inside a custom-built high-pressure supercritical reactor (SS-316), as detailed in Fig. 1. The reactor was sealed and flooded with CO_2 at 5 °C and 5 MPa. The temperature was then raised to 80 °C, and the pressure reached 15.3 MPa, where it was maintained for 6 hours. After a 45 minute depressurization, the resulting gold-doped aerogel was calcined at 300 °C for 1.5 hours, yielding an Au-impregnated aerogel (Au-AG, 3.3 g) with a purple color, indicating the presence of $AuAl_2$, consistent with the aluminum content reported in the raw aerogel.

The SS-316 reactor contains a magnetic stirrer placed beneath the metal sieve to facilitate mixing. A cooling jacket circulated a mixture of ethylene glycol and water from external circulator (Siskin Profichill RCC1200-ST40). Pressure within the reactor was monitored using a Baumer pressure transducer in conjunction with an analogue pressure gauge, while temperature was measured utilizing an RTD thermocouple. Both instruments were interfaced with a Data Acquisition (DAQ) system (Manufacturer: PPI, Mumbai, India), which was further connected to a computer running "ProLog" software for real-time recording and display of pressure and temperature readings at one-second intervals.

2.3. Analysis

FTIR spectra were acquired using IC-Agilent Cary 630 FTIR analyser. A surface characterization analysis was performed with a Brunauer–Emmett–Teller (BET) analyzer to measure the pore volume, specific surface area, and pore radius of the adsorbent. This analysis involved studying N_2 adsorption–desorption isotherms at low pressures within the 0 to 1 bar range, utilizing the JWGB Micro 122W equipment from China, installed at IIT Madras, India. Powder X-ray Diffraction (PXRD) analysis was conducted with a RIGAKU instrument, specifically the SUPERMINI FLEX 6 G BENCHTOP model. The PXRD setup was equipped with a Cu detector and D/tex ultra 2 high-speed

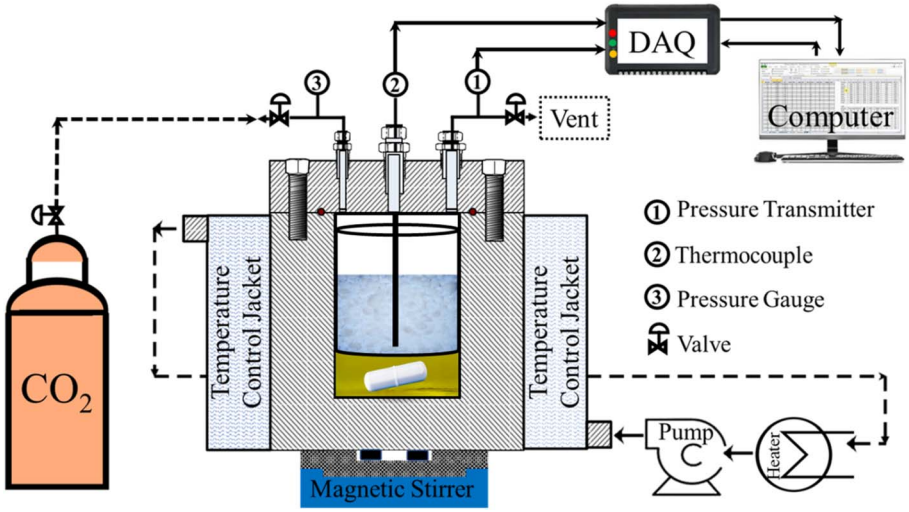

Fig. 1 Schematic diagram of the experimental setup used for the supercritical deposition of gold nanoparticles into the aerogel matrix.

silicon strip detectors, enabling coverage of 2θ ranges from −3° to +145°. Scan speeds varied from 0.01 to 100° per minute during data acquisition. SEM was conducted at Tel Aviv University using a Thermo Fisher, Quanta 200 FEG ESEM. Concentrations of Hg were determined with an Agilent 7500 ICP-MS; samples were filtered with 0.22 μm nylon filters to remove any remaining particles, then digested with 2% HCl, 5% HNO_3, and 1 ppm Au, and diluted to an expected Hg concentration below 40 ppb.

2.4. Sorption experiments

Adsorption experiments were carried out in ddH_2O spiked with $HgCl_2$ in volumes of 100 mL, using nickel foam to contain the Au-AG composite and maintain its position submerged beneath the surface of the water. Concentrations of Hg ranged between 10 ppb and 10 ppm.

A Langmuir model of adsorption was operated using eqn (1) below:

$$\frac{C_e}{Q_e} = \frac{1}{K_L Q_{max}} + \frac{C_e}{Q_{max}} \quad (1)$$

where Q_e is the adsorption capacity, K_L is the Langmuir constant, Q_{max} is the maximum adsorption capacity reached, and C_e is the equilibrium concentration at that maximum capacity.

To model the kinetics, adsorption experiments were taken over an hour at 100 ppb Hg, and the results were analyzed according to pseudo-first and pseudo-second-order kinetic models, shown below in eqn (2) and (3), respectively.

$$\log\left(Q_e^{calculated} - Q_t\right) = \log Q_e^{calculated} - \frac{k_1}{2.303} \times t \quad (2)$$

$$\frac{t}{Q_t} = \frac{1}{k_2\left(Q_e^{calculated}\right)^2} + \frac{t}{Q_e^{calculated}} \quad (3)$$

3. Results and discussion

3.1. Materials characterization

3.1.1. SEM-EDX. The silica aerogel doped with gold nanoparticles was characterized using Scanning Electron Microscopy (SEM) to examine its morphology, particle dispersion, and the structural integrity of the gold nanoparticle distribution within the aerogel matrix. The SFD (Supercritical Fluid Drying) method allowed for minimal shrinkage and structural collapse of the aerogel, which is crucial for preserving the porous framework essential to aerogel properties. The SEM images of the doped silica aerogel revealed a highly porous and interconnected network typical of aerogels. The overall structure of the silica matrix displayed a fibrous, three-dimensional network with nanoscale pores distributed uniformly throughout the sample. The SFD method effectively preserved the open-cell structure of the aerogel, resulting in a high surface area and significant porosity, which are critical factors for applications such as adsorption and catalysis.

SEM analysis revealed a broad, uniform distribution of gold nanoparticles throughout the silica aerogel matrix, with minimal aggregation. High-magnification images showed these nanoparticles were embedded within the aerogel's porous framework, often located along pore walls and bridging branches within the silica structure. The particles exhibited an average diameter of 20–40 nm, aligning well with synthesis specifications. This size range, verified through particle size distribution analysis, indicates controlled nucleation and growth during the doping process. In areas where deposition was heavier (as seen in Fig. 2a–c), the nanoparticles appeared relatively monodisperse and formed small clusters within the aerogel particles. Importantly, the gold nanoparticles were evenly dispersed without significant correlation to color variations, ruling out effects of $AuAl_2$ formation. The integration of these nanoparticles appears to enhance the aerogel's textural stability, likely due to their stabilizing influence on pore walls, thus reducing potential collapse. This high concentration of

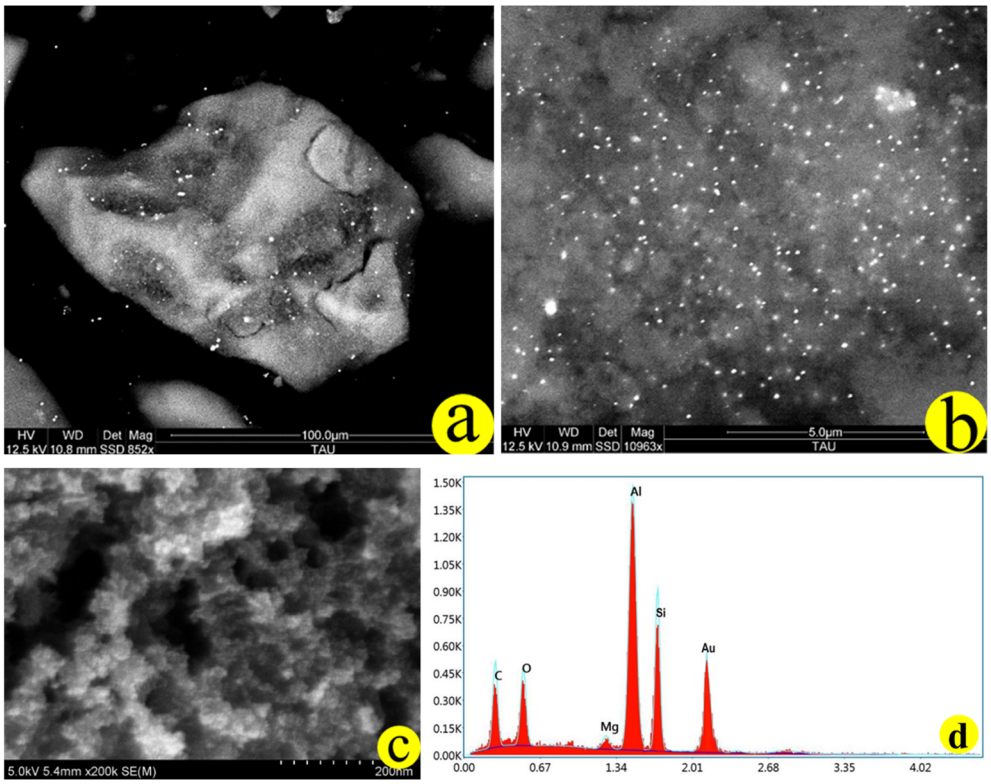

Fig. 2 SEM images of (a) the Au-AG composite showing preserved porous structure at low magnification, (b) higher magnification of the Au-AG composite revealing uniformly distributed Au nanoparticles, and (c) pristine (undoped) silica aerogel showing the mesoporous network structure in the absence of Au nanoparticles. (d) SEM-EDS spectrum of the Au-AG, showing elemental composition and peak intensities.

gold nanoparticles within the porous structure of the aerogel provides an ideal medium for applications such as mercury adsorption, leveraging the unique properties of the doped aerogel for advanced environmental and catalytic applications.

The SEM analysis confirmed that the SFD method was effective in retaining the mechanical integrity and homogeneity of the doped aerogel structure.[26] There were no observable cracks or fractures in the silica network, and the gold nanoparticles did not induce any structural disintegration. This integrity is likely due to the compatibility between the silica and gold components and the SFD technique's capability of producing an aerogel with low density and high mechanical strength. The surface texture of the silica aerogel doped with gold nanoparticles appeared smooth and consistent under SEM observation. The interface between the silica matrix and the gold nanoparticles was well-defined, indicating the successful incorporation of the nanoparticles into the aerogel network without compromising the silica matrix (Fig. 2a–c). This smooth texture suggests that the gold nanoparticles are intimately integrated within the silica framework, likely contributing to enhanced catalytic and adsorption properties by creating accessible active sites throughout the porous structure. EDS characterization of samples analyzed in SEM (Fig. 2d) indicates an elemental concentration of Au of between 13 and 20%, and the absence of Cl, thereby verifying the metallization of Au nanoparticles within the aerogel matrix. Significant concentrations of Si and O were also determined (as well as a smaller concentration of C and Al), consistent with the atomic content of the raw aerogel material.

3.1.2. X-ray diffraction. Fig. 3 showing XRD pattern of the gold-doped silica aerogel exhibited a broad, low-intensity peak centered around 2θ = 20–30°, indicative of the amorphous nature of the silica matrix. This broad hump is characteristic of non-crystalline or amorphous silica, which lacks long-range atomic order but retains a disordered, porous structure essential for aerogel properties. The amorphous matrix was

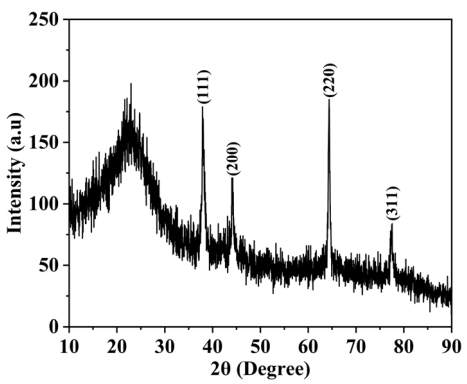

Fig. 3 XRD pattern of gold-doped silica aerogel synthesized by SFD, showing a broad peak at 2θ = 20–30° for amorphous silica and sharp peaks at 38.2°, 44.4°, 64.6°, and 77.5° indicating crystalline gold (fcc structure).

successfully preserved during the SFD process, confirming that the deposition method did not induce any crystalline transformation in the silica framework. In addition to the broad peak from the silica, sharp diffraction peaks corresponding to the crystalline structure of gold (Au) nanoparticles were observed at 2θ values of approximately 38.2°, 44.2°, 64.4°, and 77.5°. These peaks match the (111), (200), (220), and (311) planes of face-centered cubic (fcc) gold, confirming the presence of crystalline Au within the aerogel matrix. The intensity of these peaks suggests the formation of well-defined gold nanoparticles with a high degree of crystallinity.

Using the Scherrer equation, the crystallite size of the gold nanoparticles was estimated based on the width of the prominent (111) diffraction peak at $2\theta = 38.2°$. Calculations indicate an average crystallite size within the range of 20–40 nm, which aligns with particle sizes observed through SEM analysis. This consistency in size estimation further verifies that the gold nanoparticles achieved during the SFD process maintained controlled growth and retained the desired nanometer scale. The XRD analysis did not reveal any additional peaks that would indicate alloy formation or intermetallic compounds, such as Au–Si or $AuAl_2$, within the doped aerogel. The lack of such secondary phases suggests that the SFD method successfully maintained phase purity, with gold nanoparticles remaining distinct from the silica matrix. This phase purity is advantageous, as it preserves the chemical and physical properties of both the gold and the silica, essential for applications like catalysis and adsorption.

The crystallinity of gold nanoparticles embedded in the amorphous silica matrix potentially contributes to enhanced stability and durability of the aerogel structure. Gold's fcc lattice structure is inherently stable, and the strong interfacial interaction between gold and silica (observed from XRD data and corroborated by SEM analysis) suggests that the nanoparticles are well-integrated into the matrix without disrupting the aerogel's porous nature. This structural integrity further supports the aerogel's suitability for use in adsorption or catalysis applications, where stability under various conditions is critical.

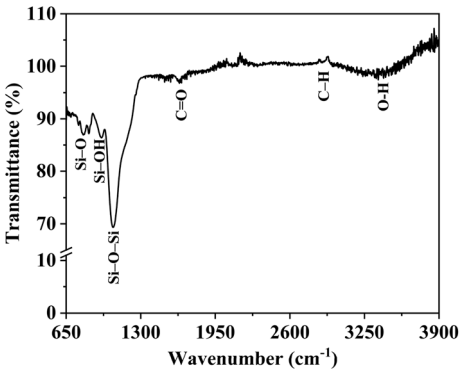

Fig. 4 FTIR spectrum of Au-AG composite from Supercritical Fluid Deposition (SFD). Peaks at ~1050 cm^{-1} and ~800 cm^{-1} confirm silica structure, while ~3400 cm^{-1} and ~1640 cm^{-1} indicate hydroxyls and adsorbed water. No Au–O–Si peaks confirm physical incorporation of gold nanoparticles without chemical bonding.

3.1.3. Fourier transform infrared spectroscopy. Fig. 4 shows the FTIR analysis of the Au-AG composite shows a broad peak around 3200–3400 cm^{-1} attributable to O–H stretching vibrations, indicating the presence of hydroxyl groups within the aerogel structure. The intensity and width of this band can provide information about the extent of hydrogen bonding and the surface hydrophobicity of the aerogels. The presence of hydroxyl groups is crucial for facilitating interactions with adsorbate and adsorbent molecules in applications of water purification. Peaks ranges from 1600–1650 cm^{-1} correspond to C=O stretching vibrations, suggesting the presence of carbonyl groups within the aerogel network. The presence of residual organic precursors or reaction byproducts containing carbonyl groups may contribute to these peaks. A strong, broad peak around 1050 cm^{-1}, attributed to the asymmetric stretching of Si–O–Si bonds, which is typical of silica aerogels. A peak around 800 cm^{-1}, indicating symmetric Si–O bending vibrations within the silica framework. A minor band near 950 cm^{-1}, representing the Si–OH surface hydroxyl groups, which are essential for maintaining the aerogel's hydrophobicity nature and surface reactivity.

Interestingly, the FTIR analysis did not reveal any new peaks associated with direct chemical bonding between the gold nanoparticles and the silica framework. This absence suggests that the gold nanoparticles were physically incorporated within the silica matrix rather than chemically bonded, consistent with their uniform dispersion and retention of phase purity observed in XRD analysis. The lack of Au–O–Si bands further indicates that the SFD method successfully retained the chemical properties of both components without inducing unintended interactions. The FTIR spectrum's consistent peaks in the silica framework and hydroxyl regions suggest that the gold nanoparticles did not disrupt the aerogel's structural or chemical stability. The presence of surface hydroxyl groups could enhance the stability of gold nanoparticles within the matrix by providing sites for hydrogen bonding or weak physical interactions, thereby maintaining nanoparticle dispersion and preventing aggregation.

3.1.4. Brunauer–Emmett–Teller (BET) isotherm. The application of supercritical CO_2 ($scCO_2$) impregnation in synthesizing the Au-AG composite offers significant structural and physicochemical advantages over conventional wet impregnation and sol–gel methods. Most notably, the composite retains a high specific surface area of 672.5 $m^2\ g^{-1}$ comparable to pristine silica aerogel, indicating negligible pore collapse or occlusion during processing. Traditional solvent-based techniques often cause capillary-induced shrinkage and densification during drying, severely reducing pore accessibility and sorption efficiency. In contrast, $scCO_2$, with its near-zero surface tension and high diffusivity, penetrates the aerogel's mesoporous structure without generating the Laplace pressures responsible for pore deformation. Its mild critical conditions (31.1 °C and ~10 MPa) further minimize thermal and mechanical stress on the matrix, enabling deep and uniform

deposition of gold precursors within the pore walls rather than superficial loading.

SEM imaging confirms that the open-pore architecture remains intact post-impregnation, while EDS mapping and spectral analysis reveal a uniform dispersion of gold nanoparticles (~18.5 wt%) throughout the aerogel. The $scCO_2$ environment supports controlled nucleation, reducing agglomeration and suppressing uncontrolled particle growth often seen in liquid-phase syntheses due to supersaturation or solubility gradients. The absence of large gold clusters suggests effective suppression of Ostwald ripening, commonly promoted by prolonged residence times in aqueous or alcoholic media. Crucially, preserving the aerogel's mesostructure is not just a structural benefit, it is essential for performance. High surface area and interconnected mesoporosity facilitate short diffusion paths and improved access to active sites, which is especially important for trace-level mercury adsorption where transport limitations prevail. By maintaining both nanostructural integrity and chemical functionality, $scCO_2$ impregnation ensures a high density of accessible chemisorptive sites and consistent adsorption performance. These advantages are further supported by previous studies,[27,28] which show that conventional deposition methods often lead to poor nanoparticle dispersion, pore blockage, and loss of structural uniformity, thereby compromising sorbent efficiency and reproducibility. Complementary BJH (Barrett–Joyner–Halenda) analysis in Fig. 5 confirms that the SFD process does not significantly alter pore volume or size distribution. The Au-AG composite exhibits a pore volume of 3.66 $cm^3\ g^{-1}$, similar to that of the undoped silica aerogel. This indicates that the SFD method effectively integrates Au nanoparticles without causing substantial filling or reduction of pore volume. The average pore size remains stable at 21.8 nm, which is beneficial for applications that require consistent pore accessibility and favorable fluid dynamics.

The isotherms of the Au-AG composite are classified as type IV, characteristic of mesoporous materials, and show minimal deviation from the undoped aerogel. This indicates that capillary condensation and pore connectivity are maintained, reflecting an intact porous structure. The presence of a consistent H1 hysteresis loop further supports the conclusion that SFD does not lead to significant structural disruption or pore blockage.

Overall, the BET analysis in Fig. 5 reveals no significant deviations in surface area, pore volume, or pore size distribution, confirming that the SFD process enables a well-dispersed integration of Au nanoparticles without obstructing the pore structure. The controlled dispersion facilitated by SFD enhances the aerogel's properties while retaining a uniform pore size distribution, which is crucial for high-performance applications. Moreover, the use of supercritical CO_2 in the SFD process allows for efficient deposition of Au nanoparticles with high penetrability into the aerogel matrix, ensuring even distribution without pore obstruction. Careful selection of precursor concentration during SFD is critical to achieving optimal Au loading while preventing excessive aggregation, thereby maintaining the integrity of the aerogel's pore structure.

3.1.5. Hg adsorption. The Au-AG composite demonstrated a high affinity for mercury, achieving a maximum adsorption capacity of 12.86 mg g^{-1} at an initial concentration of 17 ppm Hg, corresponding to a 94.2% reduction over two days. Equilibrium adsorption was reached after approximately 24 hours, with a final average removal efficiency of approximately 85%, suggesting a slower secondary diffusion- or saturation-controlled process following the rapid initial chemisorption phase. While the Langmuir-derived maximum capacity under optimized conditions is slightly higher at 12.82 mg g^{-1}, this may appear lower than values reported in some studies (*e.g.*, 200–1500 mg g^{-1}). However, such comparisons must be interpreted with caution, as those higher capacities are typically obtained at much higher initial mercury concentrations (>100 ppm) and under idealized laboratory conditions that do not reflect environmental realities. In contrast, our study focuses on ppb-level mercury concentrations, which are more representative of real-world water contamination scenarios. Under these conditions, performance indicators such as adsorption affinity, removal efficiency, and kinetics at low concentrations are more relevant than bulk capacity. Notably, the Au-AG composite achieved ~85% removal at just 17 ppb, with a rapid uptake rate ($t_{1/2}$ < 45 min), demonstrating its effectiveness and selectivity for trace-level mercury capture, where many conventional materials fail. The strong mercury binding observed is likely due to the presence of both gold and silica atoms, which are known to form stable interactions with mercury. This suggests that Au-AG composites are promising candidates for mercury removal in environmentally relevant settings.

3.1.6. Percentage Hg removed. The mercury (Hg) adsorption capacity of an Au-AG composite matrix was investigated under conditions reflecting typical pollution scenarios, with initial Hg concentrations of 17.6 ppb, 44 ppb, 100 ppb and 176 ppb shown in Fig. 6. These concentrations were treated with an Au-AG composite dosage of 0.25 g L^{-1} at a controlled temperature of 297 K. The results provide insight into the composite's efficiency, kinetics, and equilibrium characteristics in Hg removal from low-concentration solutions. The percentage of Hg removed by adsorption was consistent across

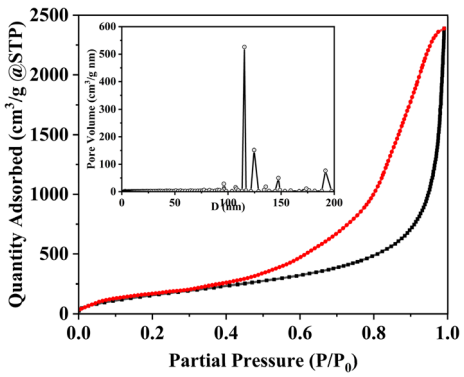

Fig. 5 BET analysis showing the surface area characteristics of the Au-AG composite.

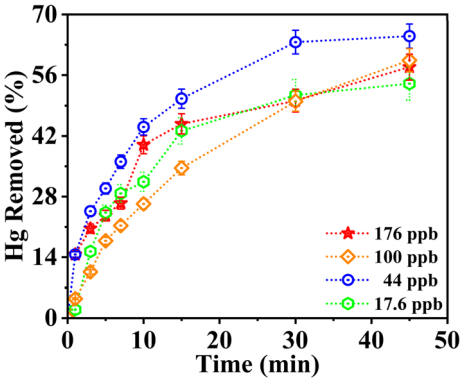

Fig. 6 Percentage removal of mercury (Hg) spiked in deionized water (ddH_2O) by the Au-AG composite at varying concentrations, illustrating the composite's effectiveness in Hg adsorption over time.

all initial concentrations tested, achieving approximately 60% removal within the first 45 minutes. This uniformity in performance, irrespective of concentration, demonstrates the composite's high affinity for Hg even at environmentally relevant, low concentrations. The initial adsorption results reflect that the Au-AG composite can effectively reduce Hg concentrations quickly, which is critical for practical applications requiring rapid removal, such as in water treatment facilities or pollution control systems.

The Au-AG composite exhibits rapid adsorption kinetics, with approximately 60% of the initial Hg content removed within the first 45 minutes. This suggests that the composite contains highly accessible active sites, likely due to chemisorption interactions between Hg ions and the Au and Ag nanoparticles embedded in the porous aerogel matrix. The large surface area and reactive sites contribute to the fast initial uptake, which is advantageous for batch purification systems requiring shorter treatment times. Despite the strong initial adsorption, equilibrium was reached only after 24 hours, with approximately 85% of the initial Hg removed and ~15% remaining in solution. In comparison, control experiments using undoped pristine silica aerogel under identical conditions showed only ~28% Hg removal, indicating primarily weak physisorption. This stark contrast highlights the critical role of gold nanoparticles in enhancing mercury capture, likely *via* Hg–Au amalgamation and chemisorption mechanisms. These results confirm that bare silica aerogel lacks sufficient affinity for effective trace-level Hg adsorption, whereas the incorporation of Au provides the necessary active sites for selective and efficient binding. The gradual approach to equilibrium suggests that while the composite has high initial capacity, complete removal requires extended contact time—possibly due to pore diffusion limitations or surface saturation effects. This behavior supports the potential for multi-stage purification processes, enabling high-purity water treatment within shorter contact durations.

The structure of the Au-AG composite likely plays a significant role in these observed adsorption dynamics. The aerogel's highly porous structure enables rapid mass transport and access to a large surface area, while the distribution of Au nanoparticles within AG matrix ensures high site availability for Hg binding. However, the slower approach to full adsorption equilibrium may indicate that some binding sites are less accessible or that the adsorption process involves multiple mechanisms (*e.g.*, surface adsorption followed by possible diffusion into micropores over time). These characteristics highlight the composite's efficiency in fast adsorption but also suggest that adjustments, such as increasing dosage or contact time, may enhance its overall effectiveness in applications where maximum Hg removal is required.

3.1.7. Langmuir isotherm. Fig. 7a illustrates the adsorption profiles of Hg^{2+} onto Au-AG composite at various initial concentrations (17.6, 44, 100, and 176 ppb), showing the variation in adsorption capacity (Q_t, μg g^{-1}) as a function of contact time over a 45 minute period. Across all concentrations, the adsorption process displays a characteristic biphasic behavior, an initial rapid uptake phase followed by a slower approach to equilibrium. This trend is attributed to the abundance of available active sites on the aerogel surface during the early stages, enabling efficient external surface adsorption. As these sites become progressively occupied, the adsorption rate decreases, likely due to increased intraparticle diffusion resistance within the mesoporous network of the aerogel. The influence of initial concentration is clearly evident: higher initial Hg(II) levels (100 and 176 ppb) led to significantly greater adsorption capacities, reaching up to approximately 460 μg g^{-1} within 45 minutes. This is a direct consequence of the increased mass transfer driving force resulting from higher solute concentrations. In contrast, at the lowest tested concentration (17.6 ppb), the adsorption capacity plateaued at a much lower value (~48 μg g^{-1}), consistent with the limited availability of mercury ions in the solution. The differences in the shape and slope of the kinetic curves further suggest that the time required to reach near-equilibrium slightly increases with concentration, reflecting the higher number of Hg^{2+} ions that must be adsorbed before saturation is approached.

The equilibrium adsorption data were analyzed using the Langmuir isotherm model shown in Fig. 7b, which assumes monolayer adsorption onto a surface with a finite number of energetically identical binding sites. This model is particularly suited for systems where chemisorption dominates and where each adsorbate molecule binds to a single adsorption site. The linearized Langmuir plot (Fig. 7b) yielded a slope of 7.799 × 10^{-5} and an intercept of 6.531 × 10^{-2}, from which the maximum adsorption capacity (Q_{max}) and the Langmuir constant (K_L) were calculated as 12.82 mg g^{-1} and 1.191 × 10^{-3} L μg^{-1}, respectively shown in Table 1. Unlike some literature reports of higher capacities obtained under artificially elevated mercury concentrations (*e.g.*, >100 ppm), the Q_{max} reported here (12.82 mg g^{-1}) reflects performance under environmentally relevant Hg levels (17.6–176 ppb), where most conventional materials fail to achieve high removal efficiency. The relatively high Q_{max} indicates the significant capacity of the Au-AG composite to adsorb mercury ions at the trace level, reflecting the contribution of well-dispersed gold nanoparticles and preserved mesoporosity. The K_L value, though moderate,

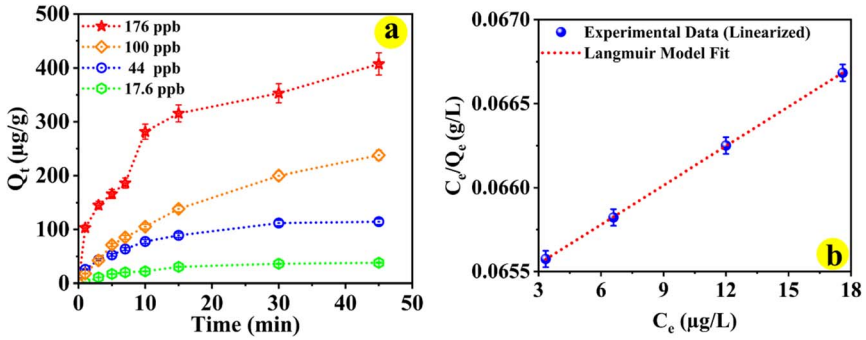

Fig. 7 (a) Adsorption kinetics of Hg ions onto Au-AG composite at varying initial concentrations (17.6, 44, 100, and 176 ppb). The adsorption capacity (Q_t, μg g^{-1}) increases rapidly in the initial phase, followed by a slower approach to equilibrium. Higher initial concentrations result in greater uptake due to increased mass transfer driving force. Error bars represent standard deviation from triplicate experiments. (b) Langmuir isotherm for Hg adsorption on Au-AG doped silica aerogel, showing monolayer adsorption with a maximum capacity $Q_{max} = 12.82$ mg g^{-1}.

Table 1 Langmuir isotherm parameters for Hg adsorption on Au-AG doped silica aerogel, including the Langmuir constant (K_L), maximum capacity (Q_{max}), and correlation coefficient (R^2)

Q_{max} (mg g^{-1})	K_L (L μg^{-1})	R_L	R^2
12.82	0.0012	0.807	0.999

suggests that the surface sites have a consistent and meaningful affinity for mercury, consistent with the strong known interaction between Hg and Au, likely driven by amalgamation or orbital hybridization effects.

To further assess the favorability of the adsorption process, the dimensionless separation factor (R_L) was calculated for trace level mercury concentration of 17.6 ppb, 44 ppb, 100pp, 176 ppb, the resulting R_L were 0.979,0.950, 0.893, and 0.826 respectively, which lies in the favorable range of $0 < R_L < 1$, indicating that the adsorption is thermodynamically feasible and efficient under the tested conditions. These results confirm that the Langmuir model provides a good description of the adsorption mechanism of Hg on the Au-AG composite, consistent with monolayer chemisorption occurring on uniformly distributed and energetically similar sites, primarily on the Au nanoparticle surfaces embedded within the silica aerogel matrix. The close model fit also suggests that the composite offers a homogeneous distribution of active binding sites, a key factor in achieving reproducible and high-efficiency adsorption, particularly at trace concentration levels. While the moderate K_L implies room for improvement in affinity, possibly through increasing Au nanoparticle loading, the current performance demonstrates a balance between capacity, accessibility, and material economy suitable for environmental mercury removal applications.

3.1.8. Kinetic analysis. The kinetics of mercury (Hg(II)) adsorption onto Au-AG composite were systematically evaluated using two widely accepted kinetic models: the pseudo-first-order and pseudo-second-order models. The experimental conditions involved trace-level initial mercury concentrations of 17.6, 44, 100, and 176 ppb, simulating realistic environmental contamination scenarios. The results, presented in Fig. 8a, b and Table 2, reveal that the adsorption kinetics vary significantly between the two models. The pseudo-second-order model exhibited an excellent fit across all concentrations, with correlation coefficients (R^2) ranging from 0.978 to 0.994. In contrast, the pseudo-first-order model yielded lower R^2 values, between 0.8565 and 0.985, and failed to accurately predict equilibrium adsorption capacities (Q_e) in several instances, particularly at higher concentrations. Pseudo-second-order

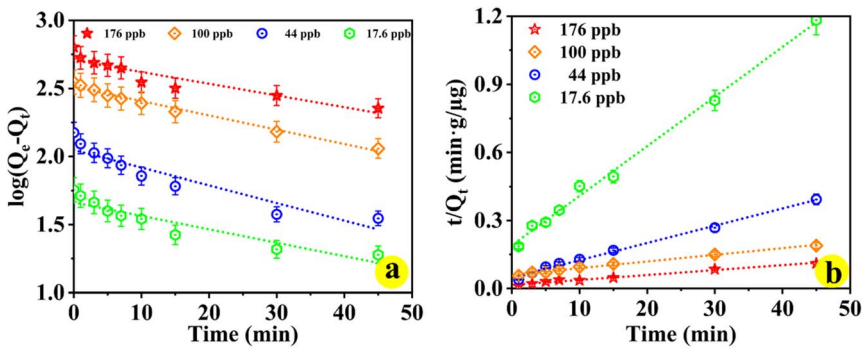

Fig. 8 (a) Pseudo-first-order kinetic model for Hg adsorption. (b) Pseudo-second-order kinetic model for Hg adsorption on Au-AG composite at concentrations of 17.6, 44, 100, and 176 ppb (0.25 g L^{-1}), demonstrating rapid chemisorption.

Table 2 Kinetic parameters for mercury (Hg) adsorption on Au-AG doped silica aerogel, including pseudo-second-order rate constant (k) and adsorption capacity (Q_e)

Initial Hg(II) (ppb)	Q_e (exp) (μg g^{-1})	Pseudo-first-order Q_e (cal)	K_1 (min^{-1})	R^2	Pseudo-second-order Q_e (cal)	K_2 (g μg^{-1} min^{-1})	R^2
17.6	48	46.05	0.00426	0.864	45.79	0.0025	0.994
44	136	111.57	0.00562	0.879	134.06	0.0012	0.993
100	340	325.84	0.00458	0.985	338.98	0.000145	0.989
176	460	510.56	0.00375	0.856	456.62	0.000313	0.978

model consistently shows much lower % error (as low as 0.30%) than the pseudo-first-order model (which reaches nearly 18% error). The close agreement between experimental and calculated Q_e values under the pseudo-second-order model strongly indicates that the rate-limiting step is governed by chemisorption, involving valence forces and potential electron sharing or exchange between mercury ions and the active sites of the gold-doped aerogel. This is consistent with the known affinity of gold for mercury, where amalgam-like interactions or strong coordination may play a role.

Moreover, the extremely high adsorption capacities observed, even at ultralow mercury concentrations, are particularly noteworthy. At just 176 ppb, the adsorbent achieved a Q_e of 460 μg g^{-1}, underscoring its exceptional performance in trace-level applications. Such behavior suggests a high density of accessible active sites and strong binding energy between the mercury ions and the Au-AG composite. The kinetic rate constants (K_2) show a decreasing trend with increasing initial Hg(II) concentrations, which may be attributed to the progressive occupation of active sites and the onset of diffusion limitations at higher loadings. Nevertheless, even at the highest concentration tested, the kinetic behavior adhered closely to the pseudo-second-order model, further affirming the robustness of the chemisorption mechanism across a range of trace-level contaminant concentrations.

4. Conclusions

This study presents a novel gold nanoparticle-doped silica aerogel (Au-AG) composite synthesized *via* supercritical CO_2 impregnation, demonstrating rapid and selective mercury (Hg) adsorption at environmentally relevant concentrations. The composite achieves 60% Hg removal within 45 minutes and reaches an adsorption capacity of 12.82 mg g^{-1}, following Langmuir isotherm behavior and pseudo-second-order kinetics, indicative of monolayer chemisorption on uniformly distributed active sites. Notably, its high performance at trace Hg concentrations, where many conventional adsorbents fail, highlights its practical relevance for environmental and drinking water applications.

Beyond efficacy, the use of commercially available Cabot P400 silica and a solvent-free, scalable supercritical process underscores the composite's potential for industrial deployment. The material's tunable Au loading capacity and high internal porosity further suggest opportunities to enhance selectivity and kinetics in future designs. These findings establish the Au-AG composite as a promising, scalable platform for trace-level mercury remediation and illustrate the broader potential of functionalized aerogels in advancing sustainable water purification technologies.

Data availability

The authors declare that the data supporting the findings of this study are available within the paper. Should any raw data files be needed in another format they are available from the corresponding author upon reasonable request.

Author contributions

All authors contributed significantly to this work. Co-first author Eitan Yosef led the conceptualization, methodology development, data collection, analysis, and drafting of the manuscript. Co-first author Subhash Kumar Sharma led methodology development, analysis, provided supervision, validated the results, wrote the original manuscript, and contributed to manuscript review and editing. Rajnish Kumar secured funding, supplied resources, reviewed the manuscript, and oversaw project administration. Hadas Mamane supported data curation, visualization, manuscript review, and formal analysis. All authors reviewed and approved the final manuscript, adhering to the journal's authorship criteria.

Conflicts of interest

There is no conflicts to declare.

Acknowledgements

This research was funded by the SPARC Programme and the Israeli Science Fund (ISF), for which we are very grateful.

References

1 C. T. Driscoll, R. P. Mason, H. M. Chan, D. J. Jacob and N. Pirrone, *Environ. Sci. Technol.*, 2013, **47**(10), 4967–4983.
2 A. Casselman, *Nature*, 2014, DOI: **10.1038/nature.2014.15680**.
3 S. Kabiri, D. N. H. Tran, S. Azari and D. Losic, *ACS Appl. Mater. Interfaces*, 2015, **7**, 11815–11823.
4 S. Wu, L. Kong and J. Liu, *Res. Chem. Intermed.*, 2016, **42**, 4513–4530.

5 F. Tadayon, M. Saber-Tehrani and S. Motahar, *Korean J. Chem. Eng.*, 2013, **30**, 642–648.
6 D. Liu, C. Lu and J. Wu, *Colloids Interfaces*, 2018, **2**, 66, DOI: 10.3390/colloids2040066.
7 K. Johari, N. Saman and H. Mat, *Environ. Technol.*, 2014, **35**, 629–636.
8 L. Zhi, W. Zuo, F. Chen and B. Wang, *ACS Sustain. Chem. Eng.*, 2016, **4**, 3398–3408.
9 T. A. Saleh, *Environ. Sci. Pollut. Res.*, 2015, **22**, 16721–16731.
10 K. P. Lisha and T. Pradeep, *Gold Bull.*, 2009, **42**, 144–152.
11 R. Ganesamoorthy, V. K. Vadivel, R. Kumar, O. S. Kushwaha and H. Mamane, *J. Clean. Prod.*, 2021, **329**, 129713.
12 N. Katagiri, M. Ishikawa, N. Adachi, M. Fuji and T. Ota, *J. Asian Ceram. Soc.*, 2015, **3**, 151–155.
13 G. Lazovski, G. Bar, B. Ji, N. Atar, U. Banin and R. Gvishi, *J. Supercrit. Fluids*, 2020, **159**, 104496.
14 K. S. Subrahmanyam, C. D. Malliakas, D. Sarma, G. S. Armatas, J. Wu and M. G. Kanatzidis, *J. Am. Chem. Soc.*, 2015, **137**, 13943–13948.
15 Y. Zhang, D. Kang, M. Aindow and C. Erkey, *J. Phys. Chem. B*, 2005, **109**, 2617–2624.
16 M. Pantić, Ž. Knez and Z. Novak, *J. Non-Cryst. Solids*, 2016, **432**, 519–526.
17 K. L. Solis, G. U. Nam and Y. Hong, *Environ. Eng. Res.*, 2016, **21**, 99–107.
18 H. Gunes, Y. Özbakir, S. B. Barim, H. Yousefzadeh, S. E. Bozbag and C. Erkey, *Front. Mater.*, 2020, **7**, DOI: 10.3389/fmats.2020.00018.
19 P. Franco, E. Pessolano, R. Belvedere, A. Petrella and I. De Marco, *J. Supercrit. Fluids*, 2023, **24**, 9269.
20 Y. Ling, S. Tan, D. Wang, J. Wu, F. Luo, Q. Liu, Y. an Zhang, F. Wang, Z. Zhang and Y. Cao, *Chem. Eng. J.*, 2022, **101**(8), 4640–4647.
21 J. Goel, K. Kadirvelu, C. Rajagopal and V. K. Garg, *J. Chem. Technol. Biotechnol.*, 2005, **80**, 469–476.
22 Z. Huang, Y. Wan, J. Liang, Y. Xiao, X. Li, X. Cui, S. Tian, Q. Zhao, S. Li and C. S. Lee, *ACS Appl. Mater. Interfaces*, 2021, **13**, 31624–31634.
23 S. Bao, K. Li, P. Ning, J. Peng, X. Jin and L. Tang, *Appl. Surf. Sci.*, 2017, **393**, 457–466.
24 E. Kokkinos, A. Lampou, I. Kellartzis, D. Karfaridis and A. Zouboulis, *Water*, 2022, **14**, 49.
25 S. K. Sharma, P. Ranjani, H. Mamane and R. Kumar, *Sci. Rep.*, 2023, **13**, 1–19.
26 A. Huerta, M. J. Torralvo, M. J. Tenorio, E. Pérez, J. Bermúdez, L. Calvo and A. Cabañas, *J. Supercrit. Fluids*, 2022, **184**, 105582.
27 B. Zhou, Z. Chen, Q. Cheng, M. Xiao, G. Bae, D. Liang and T. Hasan, *npj 2D Mater. Appl.*, 2022, **6**, 34.
28 P. D. Brown, S. K. Gill and L. J. Hope-Weeks, *J. Mater. Chem.*, 2011, **21**, 4204–4208.